Correspondence

Defect Detection in Anisotropic Plates Based on the Instantaneous Phase of Signals

Vander Teixeira Prado, Silvio Cesar Garcia Granja, Ricardo Tokio Higuti, *Member, IEEE*, Cláudio Kitano, Óscar Martínez-Graullera, *Member, IEEE*, and Luis Elvira Segura

***Abstract*—Anisotropic materials are widely employed in industry and engineering, and efficient nondestructive testing techniques are important to guarantee the structural integrity of the involved parts. A simple technique is proposed to detect defects in anisotropic plates using ultrasonic guided waves and arrays. The technique is based on the application of an objective threshold to a synthetic aperture image obtained from the instantaneous phase (IP) of the emitter-receiver signal combinations. In a previous work the method was evaluated for isotropic materials, and in this paper it is shown that with some considerations the technique can also be applied to anisotropic plates. These considerations, which should be taken into account in beamforming, are (1) group velocity dependence with propagation direction, and (2) elastic focusing, which results in energy concentration in some propagation directions, with the practical consequence that not all aperture signals effectively contribute to the image. When compared with conventional delay-and-sum image beamforming techniques, the proposed IP technique results in significant improvements relative to defect detection and artifacts/dead zone reduction.**

I. Introduction

An essential step in both structural health monitoring and nondestructive testing is damage detection, mainly when applied to composite structures. It is an area of great interest because composite structures are becoming widely applied in the aerospace and energy industries, where the use of plate-like structures demands thorough inspection due to the high safety levels of operation. To achieve this objective, the use of Lamb waves has advantages, such as relatively low attenuation, which enables testing of relatively large areas without the need to move the transducers; several propagation modes, with different sensitivities to each type of defect, so the entire thickness of a plate can be inspected, detecting surface and internal defects; and cost effectiveness [1]–[3].

Damage detection can be done by time-reversal methods [4],[5], noncontact laser ultrasonic [6], [7], changes in propagating waves [8], topological [9], and delay-and-sum (DAS) images [10], [11], and block-sparse reconstruction [12], among other techniques.

Imaging procedures with DAS [13]–[16] techniques have been reported as being effective for damage detection in composite structures [17]. In a previous work [18], the authors presented the instantaneous phase (IP) image and proposed a threshold to be applied to this image to detect defects, based on a statistical analysis of noise and the number of signals used for imaging. It is a simple method that allows the detection of multiple damages simultaneously. Defect indications in the thresholded IP image can be used as additional information for the analysis of the conventional DAS amplitude image. The method was tested with a medical phantom and an isotropic aluminum plate, resulting in improvements in reflector detectability without previous knowledge of attenuation characteristics of the propagation medium. There was also significant reduction in false indication of defects and dead zones when compared with the conventional DAS technique.

In this work, the IP technique is applied to a multilayer textile composite plain weave carbon fiber plate with artificial defects. The purpose of this paper is to show that the instantaneous phase threshold is an efficient tool for reflector detection also in anisotropic plates.

II. IP Image

By considering a linear array of M elements and amplitude time-domain data $v_{er}(t)$ obtained from all emitter (e) and receiver (r) combinations, as illustrated in Fig. 1, the IP image at point (x_0,z_0) is given by

$$I_{\varphi}(x_0,z_0) = \frac{1}{M^2}\sum_{e=1}^{M}\sum_{r=1}^{M}\varphi_{er}(\tau_{er}(x_0,z_0)), \tag{1}$$

where $\varphi_{er}(t)$ is the instantaneous phase of $v_{er}(t)$, which can be obtained by [19]:

$$\varphi_{er}(t) = \arctan\left\{\frac{\hat{v}_{er}(t)}{v_{er}(t)}\right\}, \tag{2}$$

where $\hat{v}_{er}(t)$ is the Hilbert transform of $v_{er}(t)$, and $\tau_{er}(x_0,z_0)$ is the time of flight between the transmitter e at (x_e,z_e), the point (x_0,z_0), and the receiver r at (x_r,z_r). Due to the

Manuscript received December 23, 2014; accepted July 27, 2015. This work was supported by São Paulo Research Foundation (FAPESP 2014/08790-3) and Coordination for the Improvement of Higher Education Personnel (CAPES) in Brazil, and the government of Spain (CICYT-DPI 2010-19376).

V. T. Prado is with the Department of Electrical Engineering, Universidade Tecnológica Federal do Paraná, 86399-000 Cornélio Procópio, PR, Brazil (e-mail: vanderprado@utfpr.edu.br).

S. C. G. Granja is with the Department of Mathematics, Faculdade de Ciências Exatas e Tecnológicas, Universidade do Estado de Mato Grosso, 78555-000 Sinop, MT, Brazil.

R. T. Higuti and C. Kitano are with the Department of Electrical Engineering, Faculdade de Engenharia de Ilha Solteira, Universidade Estadual Paulista, 15385-000 Ilha Solteira, SP, Brazil.

O. Martínez-Graullera and L. E. Segura are with the Instituto de Tecnologías Físicas y de la Información "Leonardo Torres Quevedo," 28006 Madrid, Spain.

DOI http://dx.doi.org/10.1109/TUFFC.2014.006955

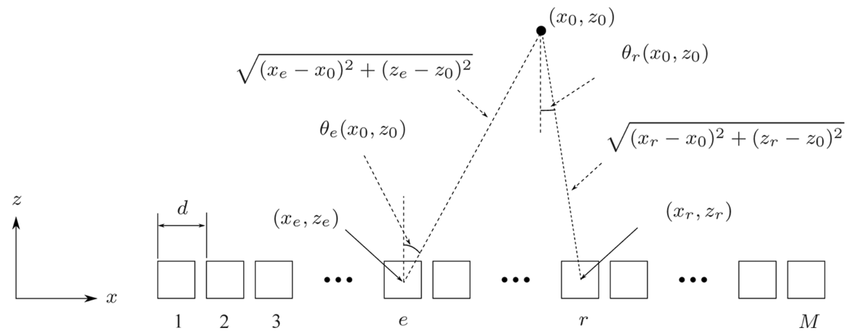

Fig. 1. Linear array with M elements, pitch d, and coordinate system.

material anisotropy, the group velocity is a function of propagation direction, and $\tau_{er}(x_0,z_0)$ is given by

$$\tau_{er}(x_0, z_0) = \frac{1}{c_{\mathrm{g}}(\theta_e(x_0, z_0))}\sqrt{(x_e - x_0)^2 + (z_e - z_0)^2} + \frac{1}{c_{\mathrm{g}}(\theta_r(x_0, z_0))}\sqrt{(x_r - x_0)^2 + (z_r - z_0)^2}, \tag{3}$$

and $c_{\mathrm{g}}(\theta_e(x_0,z_0))$ and $c_{\mathrm{g}}(\theta_r(x_0,z_0))$ are the group velocities in emitter-point and point-receiver directions, respectively. $\theta_e(x_0,z_0)$ is the angle between the array axis and the vector from the emitter position [$\theta_r(x_0,z_0)$ for receiver] to the point (x_0,z_0).

In [18], the authors defined the IP threshold as

$$\varepsilon \triangleq \frac{1}{\sqrt{\log_{10} M_{\mathrm{s}}}}, \tag{4}$$

which was obtained from a statistical analysis of noise, as a function of the number of signals used in the beamformer [M_{s}, which is equal to M^2 for (1)], and considering an isotropic medium [$c_{\mathrm{g}}(\theta_e) = c_{\mathrm{g}}(\theta_r) = c_{\mathrm{g}}$]. This threshold is not the optimum threshold (global or local), but it is a robust threshold that leads to good results for isotropic materials, when compared with empirical threshold values. For more details about this threshold definition see [18].

The image pixel is considered due to, or part of, a reflector if $|I_{\varphi}(x_0, z_0)|$ is above the threshold, and noise if it is below. In the absence of a reflector, the probability of false indication of a reflector is equal to

$$P_{\mathrm{F}} \triangleq \frac{\sigma_0^2}{M_{\mathrm{s}}} \log_{10} M_{\mathrm{s}}, \tag{5}$$

where σ_0 is the standard deviation of the instantaneous phase of the noise, which is equal to $\pi/\sqrt{3}$ rad for a uniform distribution over 2π rad.

By considering the propagation of an acoustic pressure pulsed wave, the signal at the receiver point is

$$v_{er}(t) = s_{er}(t) + n(t), \tag{6}$$

where $s_{er}(t)$ contains the reflected signals from defects and interfaces without noise, and $n(t)$ is an additive white Gaussian noise (AWGN), physically independent of the signal and therefore uncorrelated with it.

The instantaneous phase of $v_{er}(t)$ is

$$\varphi_{er}(t, x_0, z_0) = \omega t - k(\theta_e(x_0, z_0))R_e(x_0, z_0) - k(\theta_r(x_0, z_0))R_r(x_0, z_0) + \phi_{0,er} + \Delta\phi_{er}(t), \tag{7}$$

where ω is the angular frequency and for each emitter-receiver combination: $k(\theta_e(x_0,z_0))$ and $k(\theta_r(x_0,z_0))$ are the wavenumbers in emitter-point and point-receiver directions, respectively, $R_e(x_0, z_0)$ [and $R_r(x_0,z_0)$] is the distance between emitter (and receiver) and point (x_0,z_0), $\phi_{0,er}$ is the initial phase and $\Delta\phi_{er}(t)$ is a noise component.

For a propagating medium with no dispersion, or after dispersion compensation [20], [21], the group velocity is equal to the phase velocity ($c_{\mathrm{g}} = c$). Since $k = \omega/c$, then, for a nondispersive medium, $k = \omega/c_{\mathrm{g}}$ and (7) is rewritten as

$$\varphi_{er}(t, x_0, z_0) = \omega t - \frac{\omega}{c_{\mathrm{g}}(\theta_e(x_0, z_0))} R_e(x_0, z_0) - \frac{\omega}{c_{\mathrm{g}}(\theta_r(x_0, z_0))} R_r(x_0, z_0) + \phi_{0,er} + \Delta\phi_{er}(t), \tag{8}$$

which in Cartesian coordinates is equal to

$$\varphi_{er}(t, x_0, z_0) = \omega t - \frac{\omega}{c_{\mathrm{g}}(\theta_e(x_0, z_0))}\sqrt{(x_e - x_0)^2 + (z_e - z_0)^2} - \frac{\omega}{c_{\mathrm{g}}(\theta_r(x_0, z_0))}\sqrt{(x_r - x_0)^2 + (z_r - z_0)^2} + \phi_{0,er} + \Delta\phi_{er}(t). \tag{9}$$

By replacing (3) in (9), the instantaneous phase of $v_{er}(t)$ is

$$\varphi_{er}(t, x_0, z_0) = \omega t - \omega\tau_{er}(x_0, z_0) + \phi_{0,er} + \Delta\phi_{er}(t). \tag{10}$$

For each image point (x_0,z_0), the signal is summed at $t = \tau_{er}(x_0,z_0)$ for each emitter-receiver combination, which is represented in (1), and then (10) results in

$$\varphi_{er}(\tau_{er}(x_0, z_0), x_0, z_0) = \phi_{0,er} + \Delta\phi_{er}(t). \tag{11}$$

Considering that the same function is used to excite all transmitters, and supposing that all elements have the same frequency response, then $\phi_{0,er} = \phi_0$ for all M^2 transmitter-receiver combinations. Consequently, by replacing (11) in (1), the IP image at point (x_0,z_0) is

$$I_{\varphi}(x_0,z_0) = \phi_0 + I_{\Delta\phi}(x_0,z_0), \tag{12}$$

where

$$I_{\Delta\phi}(x_0,z_0) = \frac{1}{M^2}\sum_{e=1}^{M}\sum_{r=1}^{M}\Delta\phi_{er}(\tau_{er}(x_0,z_0)), \tag{13}$$

which is the same result obtained from the analysis of the IP image considering an isotropic propagating medium [18].

If there is a defect at (x_0,z_0), the image at this position $[\mathrm{I}_{\varphi}(x_0,z_0)]$ is equal to ϕ_0 plus a quantity due to noise. When there is not a defect at (x_0,z_0), the measured signal consists only of noise $n(t)$, with instantaneous phase $\phi_{\mathrm{n}}(t)$, which has uniform distribution over 2π rad [22], and the image of the pixel is related to the average of ϕ_{n} for the $M_{\mathrm{s}} = M^2$ samples. Therefore, with the analysis of the IP image and with a prior knowledge of noise, the same considerations can be done for isotropic and anisotropic materials. Then, a discrimination between reflector and noise can be done for each image pixel by the use of the threshold described in (4). The effectiveness of the proposed threshold depends on the sum of different samples of the instantaneous phase of the signals, for pixels related to defects, and noise when there is not a defect. The higher is the number of signals used in beamforming, smaller is the probability of false indication of a defect.

Besides the group velocity correction with the propagation angle, image beamforming is also influenced by the anisotropic elastic focusing effect, described by the Maris factor [23], [24]. As presented in [23], the wave intensity in the propagation path is reduced by $\sqrt{|Ak\cos\theta_{\mathrm{d}}|}$, where the angle θ_{d} is the difference between group and phase velocities directions, and A is defined as

$$A = \frac{1}{K_{\mathrm{s}}\sqrt{s^2 + \left(\frac{\mathrm{d}s}{\mathrm{d}\theta}\right)^2}}, \tag{14}$$

where s is the slowness curve, given by $s = k/\omega$, θ is $\theta_e(x_0,z_0)$ in transmission and $\theta_r(x_0,z_0)$ in reception, and K_{s} is the curvature of the slowness curve.

Also according to [23] and [25], there are many reasons for the dependence of the signal amplitude with propagation direction. However, the focusing factor A is generally dominant in highly anisotropic materials. The anisotropic elastic focusing is a characteristic of the material, and the energy of a wave is concentrated in some sectors, due to fiber orientation, for example. Consequently, it will be possible to obtain an image of the anisotropic structure, with good SNR, only in a limited region in front of the array.

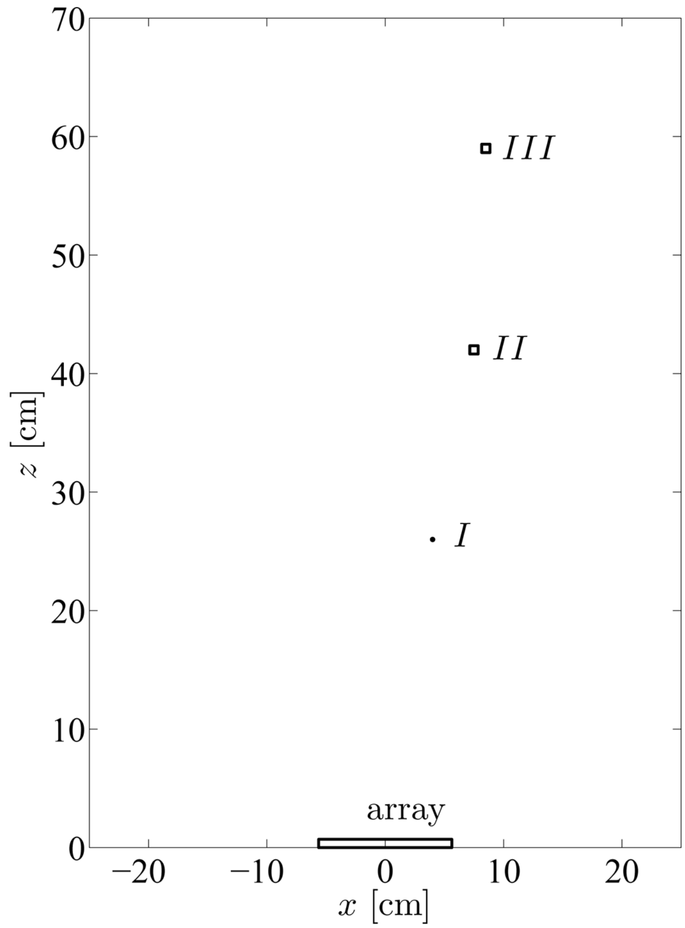

Fig. 2. Plate with defects.

III. Experimental Results

A linear array consisting of 16 PZT elements (7 × 6 × 0.5 mm; PZ26, Ferroperm Piezoceramics A/S, Kvistgaard, Denmark) polarized in the thickness direction with 7.5-mm pitch is mounted at the border of a 2-mm-thick (50 × 70 cm), nine-layer carbon fiber composite plate with artificial defects, as illustrated in Fig. 2. The fiber material in each individual ply is T300/F155 pre-preg plain woven fabric. The nine layers present the following orientations: $0°/90°/45°/90°/0°/90°/-45°/90°/0°$ with orthotropic symmetry. The elastic constants of the material are shown in Table I.

Three defects were produced on the plate: defect *I* is a 2-mm-diameter through-hole and defects *II* and *III* are PZT ceramics similar to the ones used in the array, which were bonded to the structure for tests such as frequency response and propagation velocity measurement. The artificial defects are shown schematically in Fig. 2.

TABLE I. Elastic Parameters for Each Individual Ply T300/F155 Pre-Preg Plain Woven.

$C_{11} = C_{22}$ (GPa)	C_{12} (GPa)	$C_{13} = C_{23}$ (GPa)	C_{33} (GPa)	$C_{44} = C_{55}$ (GPa)	C_{66} (GPa)	Mass density (10^3 kg/m^3)
61.69	6.962	8.621	12.36	2.767	12.01	1.56

The array elements are excited by a waveform generator (14-bit resolution; AFG3101, Tektronix Inc., Beaverton, OR, USA) and a power amplifier (40 W; 240L, Electronics and Innovation Ltd., Rochester, NY, USA) with a 100-V peak-to-peak four-cycle Gaussian envelope RF signal. Data acquisition is done using a digital oscilloscope (10 bits resolution in average mode; MSO7014B, Agilent Technologies Inc., Santa Clara, CA, USA), with average of 16 signals for each recorded waveform. A 32-channel multiplexer is used to obtain all transmit-receive combinations employed in the beamforming techniques.

Considering the elastic constants presented in Table I, the theoretical anisotropic plate dispersion curves can be obtained, as described by [26]. Using a pair of PZT elements (defects *II* and *III*), one as transmitter and the other as receiver, the frequency response was experimentally measured, and the amplitude of the S0 mode was found to be much higher than the A0 mode at the frequency of 310 kHz. Fig. 3 illustrates a time history signal at 310 kHz. By the previous knowledge of the element position (considering the center of each ceramic) and propagation velocity, the time of flight of the direct signal and some reflections can be estimated, as indicated in Fig. 3 (S0 mode: approximately 34.5 μs for the direct signal, 70 μs for the reflection related to the plate-end at z-direction, and 77 μs for the lateral plate-end reflection; A0 mode: approximately 136 μs for the direct signal). As expected, no considerable dispersion is observed in these signals. The A0 mode is present, but with very small amplitude. Furthermore, as the S0 mode velocity is considered in the beamformer, the small-amplitude A0 mode signals are summed out of phase, resulting in small artifacts that are suppressed by the IP method. From these information, the S0 mode at 310 kHz was chosen due to its low dispersive characteristic and quasi-single mode operation.

The theoretical group velocity dependence with propagation angle is shown in Fig. 4(a) for this mode. There is a variation of almost 10% in the group velocity from 0°

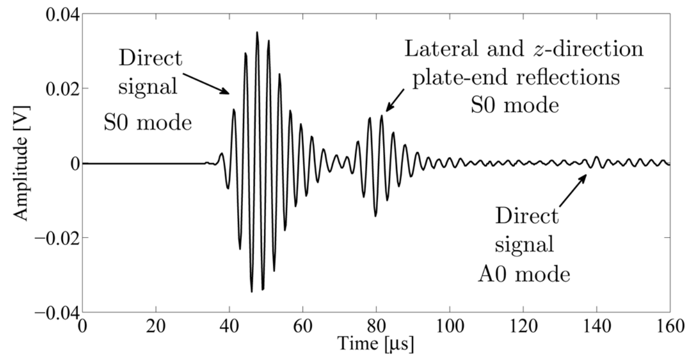

Fig. 3. Time history signal used in initial tests illustrating the quasi-single mode operation of the nondispersive S0 mode. Transmitter and receiver ceramics positions are indicated as defects *II* and *III* in Fig. 2, respectively.

to 45°, which should be considered in beamforming. The anisotropic elastic focusing, represented by the Maris factor, results in amplitude reduction for some angle directions, which was theoretically calculated for this plate, as illustrated in Fig. 4(b). An experimental test was conducted to endorse this characteristic, as previously done by [27], where the same behavior was qualitatively obtained.

From Fig. 4(b), there is a reduction in the amplitude values by a factor of 0.48 in the propagation direction of 45°. By considering the propagation path from the emitter to a point located in this direction, respect to the emitter, and back to the receiver, the reduction factor is equal to $(0.48)^2 = 0.23$. By exciting the PZTs with a 100-V peak-to-peak signal, the measured echo signals, in the best case (0°), have 30 mV peak-to-peak, for this particular setup. Considering a reduction factor of 0.23, it can be concluded that at 45° the measured signal consists only of noise. If these signals are considered in beamforming, the image SNR will be reduced. Using the same procedure as in [14], an empirical solution to reduce this effect ignores the contribution of any transmit-receive pairs where either the incident or the reflected path has an angle that is

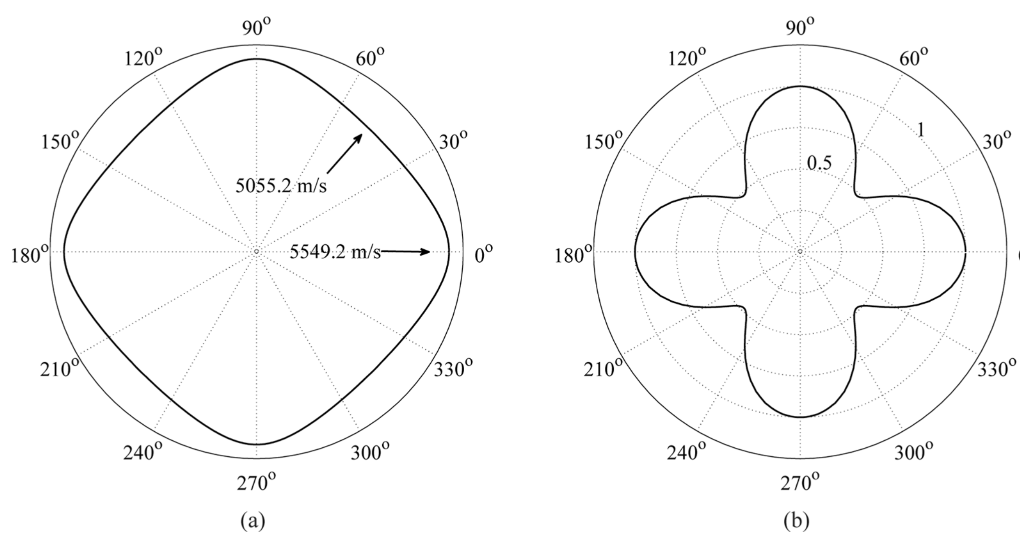

Fig. 4. (a) Group velocity and (b) normalized amplitude reduction due to the Maris factor, as functions of the propagation direction for the S0 mode at 310 kHz.

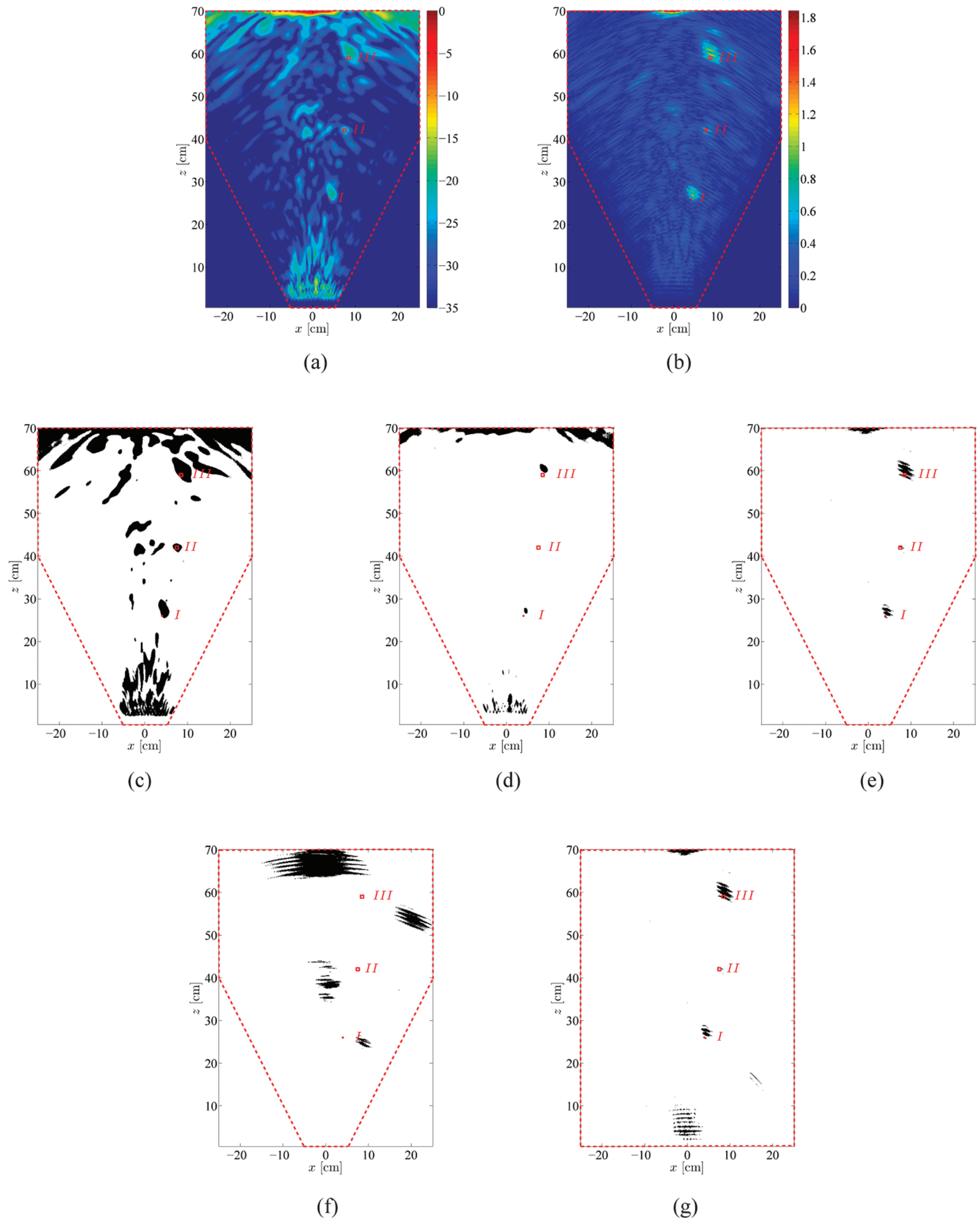

Fig. 5. Images of the plate: (a) amplitude image (scale in dB); (b) IP image (scale in rad); thresholded amplitude image by threshold values of (c) 5% and (d) 10%; (e) thresholded IP image ($\varepsilon = 0.6444$ rad); thresholded IP image (f) for constant group velocity and (g) without θ_{lim} (but considering the dependence of group velocity with angle). Image area is limited by the red dashed lines, due to θ_{lim}.

greater than some specified limit, θ_{lim}. From Fig. 4(b), the amplitude is reduced by 3 dB for $\theta = 30°$. Therefore, in this work, for any point whose angle between emitter and image point or receiver and image point is greater than 30°, the respective signal is not considered in the image beamforming.

Fig. 5 presents the resulting images using DAS amplitude and IP images, considering the dependence of group velocity with angle, as illustrated Fig. 4(a). Actual defect sizes and positions are represented by red markers. The image area is limited by $\theta_{\text{lim}} = 30°$, as indicated by dashed lines in the images. The amplitude image, which is illustrated in Fig. 5(a), was obtained by using the amplitude information instead of the instantaneous phase in (1), which is the original total focusing method (TFM) [28]. An empirical exponential time-gain compensation was applied to the time-domain signals to equalize the level of the defects. All defects are represented in the image, but there are artifacts in the compensated image with similar intensities to the true defects. The IP image, by using (1), is illustrated in Fig. 5(b).

The amplitude image was thresholded for producing a defect indicator. Figs. 5(c) and 5(d) present the thresholded amplitude image considering 5% and 10% threshold values, respectively. Using 5% of the maximum pixel intensity as threshold, all reflectors are detected. On the other hand, there are several false indications of defects. By considering a 10% threshold, artifacts are reduced,

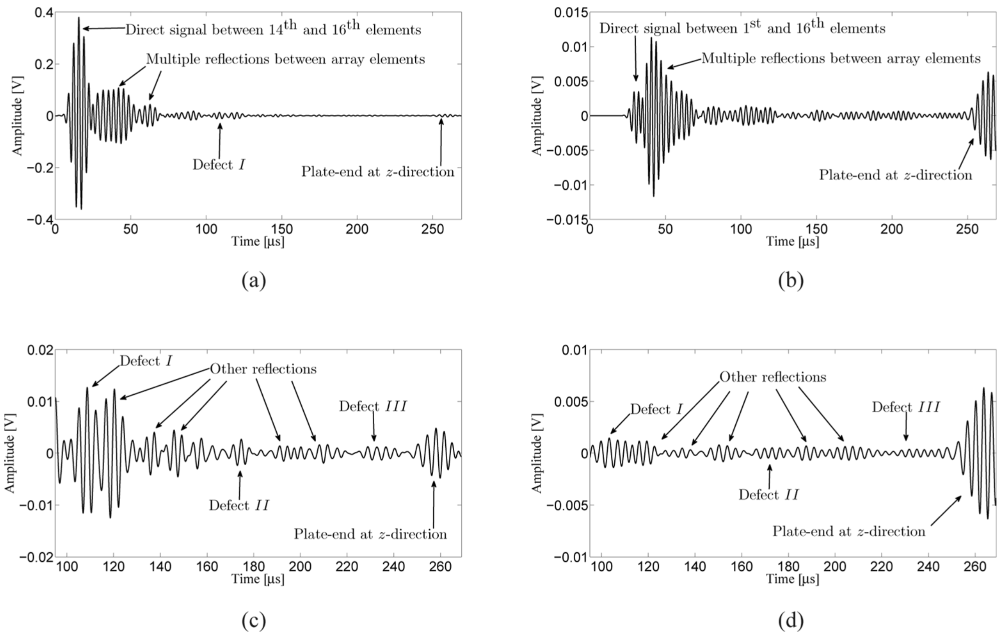

Fig. 6. Time history signals for transmitter-receiver pair as (a) 14th to 16th and (b) 1st to 16th array elements. Zoom in the time interval with defects reflections: (c) 14th to 16th and (d) 1st to 16th pairs.

but defect *II* is not represented in the two-level image. Other threshold values were also considered, and using 20% threshold, for example, no defect is detected. Consequently, even with distance compensation, the improper selection of threshold value results in incorrect evaluation of the structure.

The thresholded IP image, considering the threshold value described in (4), is illustrated in Fig. 5(e). For this setup the threshold is equal to 0.6444 rad. As can be observed, all reflectors are detected and dead zone is eliminated. The plate-end at z-direction can also be observed. Defect *II* resulted in a smaller indication, probably due to weak bonding of the defect to the plate.

Fig. 5(f) illustrates the thresholded IP image for the case when the group velocity is considered constant and Fig. 5(g) for the case when all signal combinations are used in beamforming, that is, $\theta_{\text{lim}} = 90°$ (but using the dependence of group velocity with angle). The first presents artifacts, and no defect is present in its actual position. The second presents all defects, but with some false indications and dead zone. Therefore, the IP threshold is also valid for anisotropic plates, but it is important that two characteristics are taken into account: (1) the dependence of group velocity with respect to the propagation direction; and (2) the Maris factor, to consider only the signals that effectively contribute to image beamforming, inside a propagation angle. Dispersion compensation was not necessary because the S0 mode with low dispersive characteristic (at 310 kHz) was used. If a high dispersive mode is used, then dispersion compensation should be considered.

All defects are smaller than the wavelength. Defect *I* (diameter) is around eight times smaller than the wavelength, whereas defects *II* and *III* are smaller than half-wavelength. In the resulting images, the pixel areas related to defect representation are larger than the real defects, and no information about defect sizes and geometries can be provided. The IP method [18] has the objective of improving defect detection and not exactly defect characterization.

In composite materials, signal attenuation is an important issue and can limit the maximum range of inspection. Actually, this is more critical when the amplitude is used in beamforming, when compared with the IP technique. Fig. 6 illustrates two time history signals related to two emitter-receiver pairs with different relative positions: 14th to 16th elements and 1st to 16th elements. By having previous knowledge of the array element position (center of each ceramic), propagation velocity, and defect location, it is possible to localize several echoes: direct signal (lateral emission from element to element), multiple reflections between array elements superposed to the direct signal, defect reflections (direct and multiple), and plate-end reflections.

Although the viscoelastic damping is also anisotropic, the signal-to-noise ratio is still acceptable after a travel distance of up to 1.5 m. Otherwise, it would not be possible to observe the plate-end at z-direction in both signals [Figs. 6(c) and 6(d)]. It is important to highlight that the waveforms in Fig. 6 are not plotted in the same vertical scale (i.e., for the 1st to 16th elements the amplitude of reflections is smaller than the observed for the 14th to 16th pair elements). However, all reflectors can be observed in the images as a result of the improvement in SNR due to the averaging effect of the TFM [28]. Furthermore, if the amplitude is very small but it is still possible to extract the instantaneous phase of the signal, then the IP method can be applied.

IV. Conclusion

The threshold based on the instantaneous phase of the array aperture data was applied to an anisotropic plate with artificial defects. By considering that the group velocity is a function of the propagation direction and limiting the image area, based on the Maris factor, defect detection is significantly improved when compared with the use of empirical threshold values in the amplitude image. A threshold value that results in correct detection of all reflectors for the amplitude images may exist, but this value is empirical and depends on the experimental conditions. Therefore, the IP threshold is a good tool for reflector detection also in anisotropic plates, and can be used as additional and valuable information to improve conventional amplitude image analysis. The focus of the experimental tests was to validate the IP method in an anisotropic plate. Thereby simple defects were considered. In future works, the technique will be tested in plates with delaminations to assess the sensitivity of the method to this type of damage. Furthermore, alternative methods will be investigated to overcome the angle limitation, to inspect the complete plate and not only the area in front of the array.

References

[1] D. N. Alleyne and P. Cawley, "The interaction of Lamb waves with defects," *IEEE Trans. Ultrason. Ferroelectr. Freq. Control*, vol. 39, no. 3, pp. 381–397, 1992.

[2] J. L. Rose, "Guided wave nuances for ultrasonic nondestructive evaluation," *IEEE Trans. Ultrason. Ferroelectr. Freq. Control*, vol. 47, no. 3, pp. 575–583, 2000.

[3] Z. Su, L. Ye, and Y. Lu, "Guided Lamb waves for identification of damage in composite structures: A review," *J. Sound Vibrat.*, vol. 295, no. 3–5, pp. 753–780, 2006.

[4] A. J. Devaney, "Time reversal imaging of obscured targets from multistatic data," *IEEE Trans. Antenn. Propag.*, vol. 53, no. 5, pp. 1600–1610, 2005.

[5] C. H. Wang, J. T. Rose, and F.-K. Chang "A synthetic time-reversal imaging method for structural health monitoring," *Smart Mater. Struct.*, vol. 13, no. 2, pp. 415–423, 2004.

[6] B. Park, H. Sohn, P. H. Malinowski, and W. Ostachowicz, "Damage detection in composites by noncontact laser ultrasonic," in *7th European Workshop on Structural Health Monitoring*, Nantes, 2014, pp. 340–347.

[7] C. Zhang, J. Qiu, and H. Ji, "Laser ultrasonic imaging for impact damage visualization in composite structure," in *7th European Workshop on Structural Health Monitoring*, Nantes, 2014, pp. 2199–2205.

[8] M. RadzieńskiL. Doliński, M. Krawczuk, and M. Palacz, "Damage localisation in a stiffened plate structure using a propagating wave," *Mech. Syst. Signal Process.*, vol. 39, no. 1–2, pp. 388–395, 2013.

[9] S. Rodriguez, M. Castaings, M. Deschamps, and E. Ducasse, "Topological imaging of defects in anisotropic plates," in 7th European Workshop on Structural Health Monitoring, Nantes, 2014, pp. 1155–1162.

[10] P. Fromme, P. D. Wilcox, M. J. Lowe, and P. Cawley, "On the development and testing of a guided ultrasonic wave array for structural integrity monitoring," *IEEE Trans. Ultrason. Ferroelectr. Freq. Control*, vol. 53, no. 4, pp. 777–785, 2006.

[11] J. E. Michaels, "Detection, localization and characterization of damage in plates with an *in situ* array of spatially distributed ultrasonic sensors," *Smart Mater. Struct.*, vol. 17, no. 3, art. no. 035035, 2008.

[12] R. M. Levine and J. E. Michaels, "Block-sparse reconstruction and imaging for Lamb wave structural health monitoring," *IEEE Trans. Ultrason. Ferroelectr. Freq. Control*, vol. 61, no. 6, pp. 1006–1015, 2014.

[13] L. J. Busse, "Three-dimensional imaging using a frequency-domain synthetic aperture focusing technique," *IEEE Trans. Ultrason. Ferroelectr. Freq. Control*, vol. 39, no. 2, pp. 174–179, 1992.

[14] C. Li, D. Pain, P. D. Wilcox, and B. W. Drinkwater, "Imaging composite material using ultrasonic arrays," *NDT Int.*, vol. 53, pp. 8–17, 2013.

[15] R. Sicard, J. Goyette, and D. Zellouf, "A SAFT algorithm for Lamb wave imaging of isotropic plate-like structures," *Ultrasonics*, vol. 39, no. 7, pp. 487–494, 2002.

[16] M. Spies and W. Jager, "Synthetic aperture focusing for defect reconstruction in anisotropic media," *Ultrasonics*, vol. 41, no. 2, pp. 125–131, 2003.

[17] Z. Sharif-Khodaei and M. H. Aliabadi, "Assessment of delay-and-sum algorithms for damage detection in aluminium and composite plates," *Smart Mater. Struct.*, vol. 23, no. 7, art. no. 075007, 2014.

[18] V. T. Prado, R. T. Higuti, C. Kitano, and O. Martínez-Graullera, "Instantaneous phase threshold for reflector detection in ultrasonic images," *IEEE Trans. Ultrason. Ferroelectr. Freq. Control*, vol. 61, no. 7, pp. 1204–1215, 2014.

[19] A. V. Oppenheim, R. W. Schafer, and J. R. Buck, *Discrete-Time Signal Processing*. Upper Saddle River, NJ, USA: Prentice Hall, 1999.

[20] P. D. Wilcox and P. Cawley, "The effect of dispersion on long-range inspection using ultrasonic guided waves," *NDT Int.*, vol. 39, no. 1, pp. 1–9, 2001.

[21] P. D. Wilcox, "A rapid signal processing technique to remove the effect of dispersion from guided wave signals," *IEEE Trans. Ultrason. Ferroelectr. Freq. Control*, vol. 50, no. 4, pp. 419–427, 2003.

[22] A. B. Carlson and P. B. Crilly, *Communication Systems*. New York, NY, USA: McGraw-Hill Higher Education, 2009.

[23] B. Chapuis, N. Terrien, and D. Royer, "Modeling and experimental investigations of Lamb waves focusing in anisotropic plates," *J. Phys. Conf. Ser.*, vol. 269, art. no. 012020, 2011.

[24] H. J. Maris, "Enhancement of heat pulses in crystals due to elastic anisotropy," *J. Acoust. Soc. Am.*, vol. 50, 3B, pp. 812–818, 1971.

[25] D. Royer, "Mixed matrix formulation for the analysis of laser-generated acoustic waves by a thermoelastic line source," *Ultrasonics*, vol. 39, no. 5, pp. 125–131, 2003.

[26] L. Wang and F. G. Yuan, "Group velocity and characteristic wave curves of Lamb waves in composites: Modeling and experiments," *Compos. Sci. Technol.*, vol. 67, no. 7–8, pp. 1370–1384, 2007.

[27] B. Chapuis, N. Terrien, and D. Royer, "Excitation and focusing of Lamb waves in a multilayered anisotropic plate," *J. Acoust. Soc. Am.*, vol. 127, no. 1, pp. 198–203, 2010.

[28] C. Holmes, B. W. Drinkwater, and P. D. Wilcox, "Post-processing of the full matrix of ultrasonic transmit-receive array data for nondestructive evaluation," *NDT Int.*, vol. 38, no. 8, pp. 701–711, 2005.